Technical note

Seller Oria, Carmen; Free, Jeffrey; Marmitt, Gabriel Guterres; Knäusl, Barbara; Brandenburg, Sytze; Knopf, Antje C.; Meijers, Arturs; Langendijk, Johannes A.; Both, Stefan

Published in:
Medical Physics

DOI:
10.1002/mp.16208

Publication date:
2023

Advanced, Independent SRS & SBRT QA Solutions

NEW

SunSCAN™ 3D Water Scanning System

StereoPHAN™, SRS MapCHECK®, MultiMet-WL Cube

Meet the stringent demands of stereotactic treatments, with our suite of SRS/SBRT solutions.

Learn more: sunnuclear.com/srsqa

MR Distortion & Image Fusion Head Phantom

STEEV™ Phantom

sunnuclear.com

The SunSCAN 3D system is not available for sale in all markets. CE mark pending.

SUN NUCLEAR
A MIRION MEDICAL COMPANY

Received: 10 January 2022 | Revised: 19 December 2022 | Accepted: 20 December 2022

DOI: 10.1002/mp.16208

TECHNICAL NOTE

MEDICAL PHYSICS

Technical note: Flat panel proton radiography with a patient specific imaging field for accurate WEPL assessment

Carmen Seller Oria[1] | **Jeffrey Free**[1] | **Gabriel Guterres Marmitt**[1] | **Barbara Knäusl**[2] | **Sytze Brandenburg**[1] | **Antje C. Knopf**[1,3] | **Arturs Meijers**[1,4] | **Johannes A. Langendijk**[1] | **Stefan Both**[1]

[1]Department of Radiation Oncology, University Medical Center Groningen, University of Groningen, Groningen, The Netherlands

[2]Department of Radiation Oncology, Medical University of Vienna, Vienna, Austria

[3]Department of Internal Medicine, Center for Integrated Oncology Cologne, University Hospital of Cologne, Cologne, Germany

[4]Center for Proton Therapy, Paul Scherrer Institute, Villigen, Switzerland

Correspondence
Carmen Seller Oria, Department of Radiation Oncology, University Medical Center Groningen, PO Box 30001, 9700 RB Groningen, The Netherlands.
Email: c.seller.oria@umcg.nl

Funding information
KWF Kankerbestrijding (Dutch Cancer Society): 11518

Abstract

Background: Proton radiography (PR) uses highly energetic proton beams to create images where energy loss is the main contrast mechanism. Water-equivalent path length (WEPL) measurements using flat panel PR (FP-PR) have potential for in vivo range verification. However, an accurate WEPL measurement via FP-PR requires irradiation with multiple energy layers, imposing high imaging doses.

Purpose: A FP-PR method is proposed for accurate WEPL determination based on a patient-specific imaging field with a reduced number of energies (n) to minimize imaging dose.

Methods: Patient-specific FP-PRs were simulated and measured for a head and neck (HN) phantom. An energy selection algorithm estimated spot-wise the lowest energy required to cross the anatomy (Emin) using a water-equivalent thickness map. Starting from Emin, n was restricted to certain values (n = 26, 24, 22, …, 2 for simulations, n = 10 for measurements), resulting in patient-specific FP-PRs. A reference FP-PR with a complete set of energies was compared against patient-specific FP-PRs covering the whole anatomy via mean absolute WEPL differences (MAD), to evaluate the impact of the developed algorithm. WEPL accuracy of patient-specific FP-PRs was assessed using mean relative WEPL errors (MRE) with respect to measured multi-layer ionization chamber PRs (MLIC-PR) in the base of skull, brain, and neck regions.

Results: MADs ranged from 2.1 mm (n = 26) to 21.0 mm (n = 2) for simulated FP-PRs, and 7.2 mm for measured FP-PRs (n = 10). WEPL differences below 1 mm were observed across the whole anatomy, except at the phantom surfaces. Measured patient-specific FP-PRs showed good agreement against MLIC-PRs, with MREs of 1.3 ± 2.0%, −0.1 ± 1.0%, and −0.1 ± 0.4% in the three regions of the phantom.

Conclusion: A method to obtain accurate WEPL measurements using FP-PR with a reduced number of energies selected for the individual patient anatomy was established in silico and validated experimentally. Patient-specific FP-PRs could provide means of in vivo range verification.

KEYWORDS
adaptive proton therapy, flat panel detector, proton radiography, range verification, water equivalent path length

1 | INTRODUCTION

Range probing and proton radiography (PR) correspond to an ion-based imaging modality that exploits the transmission of high-energy proton beams through a patient to generate images in which the main contrast mechanism is the energy loss.[1] In proton therapy, PR allows using of the same particle for treatment and for imaging purposes, overcoming the uncertainties arising from the conversion of CT numbers into relative stopping power.[2–5] Several studies have proven the suitability of PR to detect and/or mitigate multiple sources of range uncertainty such as patient misalignments, CT calibration curve errors, or anatomical variations.[4,6–11] In the context of adaptive proton therapy, PR has a potential role as a quality control tool that provides in vivo range verification measurements. PR could assist decisions upon plan adaptation in combination with other daily x-ray-based imaging modalities.[12,13]

PR detector configurations, initially developed for double-scattering proton therapy systems, are classified into list and integration modes. List mode configurations consist of upstream and/or downstream trackers, which record the trajectory of particles individually, and a residual energy detector at the beam exit of the patient.[14,15] Such configurations can provide accurate water equivalent path length (WEPL) measurements, although they result in complex and bulky clinical implementation.[1,16,17] On the contrary, integrating systems are more compact and cost-effective in terms of adoption in clinical practice. They rely on a single detector located distally to the patient, which records a signal integrated over a large number of incident protons. Scintillator screens with a charge-coupled device, diode arrays, or amorphous silicon detectors are examples of detectors used for PR integrating systems.[16,18,19] Integrating systems do not allow to reconstruction of the trajectory of individual particles, therefore they provide images with a lower spatial resolution as compared to list mode configurations. Nonetheless, integrating systems are worth investigating for in vivo range verification, where the key is not to have high resolution spatially but rather in the beam eye's direction, to achieve accurate residual range or WEPL measurements.

With the increasing prevalence of pencil beam scanning over double-scattering proton therapy systems, new PR detector solutions have emerged. PR with a single pencil beam energy and a multi-layer ionization chamber (MLIC-PR), also known as range probing, has proven to be suitable as a quality control tool to detect multiple sources of range errors.[6,7,10,20,21] Furthermore, MLIC-PR has enabled in vivo proton range verification in head and neck (HN) cancer patients.[12,13]

Flat panel (FP) detectors suitable for proton radiation offer the most compact integrating PR solution, as well as large readout areas. Therefore, PR with a FP (FP-PR) could be used for in vivo range verification in adaptive workflows. Due to the small thickness of FPs, WEPL measurements by means of FP-PR rely on imaging fields composed of several energy layers.[22–25] The acquisition of WEPL values by FP-PR was first proposed by Bentefour et al., who introduced the concept of energy resolved dose functions (ERDF).[23] An ERDF represents the change in the FP signal as a function of different initial pencil beam energies composing the PR field.[23] Previous studies showed how to retrieve WEPL by comparing the ERDFs obtained from a PR acquisition against a set of ERDFs measured for known water equivalent thicknesses (WET).[17,22,24,26]

To lower imaging dose and delivery time, various FP-PR studies reduced the number of energy layers by increasing the energy spacing, causing a loss of WEPL accuracy unacceptable for in vivo range verification.[17,22,24,27] In addition, previous FP-PR studies suggested the need for a strategy to choose energy layers using prior patient information like a planning CT.[17,22,24,26,27] However, research up to date has not yet resulted in a solution to efficiently reduce the imaging dose of FP-PRs.

To avoid compromising on WEPL accuracy, this work proposes an alternative imaging dose reduction solution that does not increase the energy spacing. Instead, the energy spacing is kept constant and the imaging dose reduction is achieved by excluding spots with low energies that would stop inside the anatomy, as well as spots with very high energies that have low relevance for the WEPL reconstruction. A spot-wise energy selection algorithm to acquire FP-PRs with an imaging field tailored to the individual anatomy was proposed in silico and validated experimentally.

2 | MATERIALS AND METHODS

A spot-wise energy selection algorithm was developed to minimize the imaging dose imposed by FP-PR. The images resulting from the energy selection algorithm are called "patient specific FP-PRs." In Section 2.1. the energy selection algorithm is presented, and its performance is evaluated against conventional FP-PRs, referred to as "reference FP-PRs." This analysis is performed via simulations as well as measurements. In Section 2.2., the WEPL accuracy of patient specific FP-PRs is evaluated by comparing MLIC-PR, considered as ground truth in terms of WEPL accuracy, against patient specific and reference FP-PRs. This section contains a quantification of WEPL accuracy with simulated as well as experimental results. Table 1 guides the reader through the data generated in this study, summarizing the main features of all PRs simulated and measured in each section.

TABLE 1 Summary of all PRs performed via simulations and measurements in each section. Details on the field size, field position and the kind of PR that was performed (MLIC-PR, reference FP-PR, or patient specific FP-PR) are specified for each case

Section	Data type	Data comparison	Field size (cm^2)	Field position
2.1	Simulation	Reference FP-PR vs. patient specific FP-PR (n = 26, …., 2)	27 × 27	Isocenter
	Measurement	Reference FP-PR vs. patient specific FP-PR (n = 10)	27 × 27	Isocenter
2.2.	Simulation	MLIC-PR vs. reference, patient specific FP-PR (n = 26, …, 2)	4 × 4	Base of skull, neck, brain
	Measurement	MLIC-PR vs. reference, patient specific FP-PR (n = 10)[a]	4 × 4	Base of skull, neck, brain

[a]Cropped regions from the FP-PRs measured with a 27 × 27 cm^2 field.

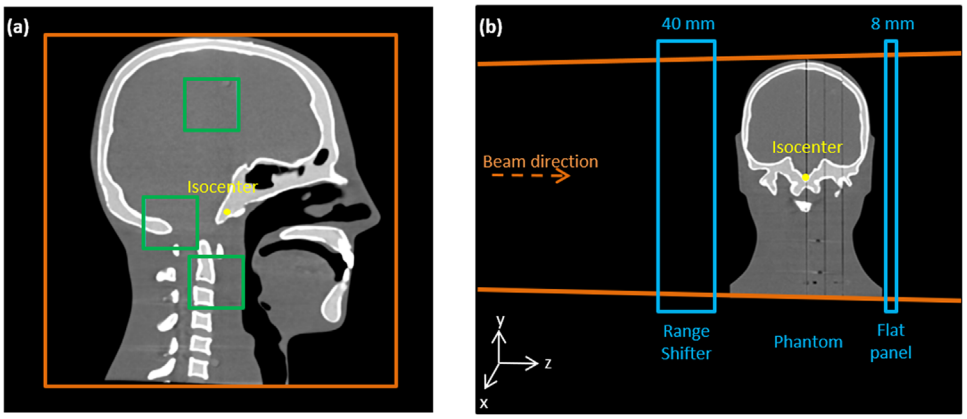

FIGURE 1 (a) Sagittal plane of the HN phantom. A FP-PR imaging field of 27 × 27 cm^2 is highlighted in orange (a1), centered at the isocenter (yellow). Three small FP-PR fields of 4 × 4 cm^2 in the brain, base of skull and neck are highlighted in green (a2, a3, a4). These regions are used to compare FP-PR against MLIC-PR. (b) Schematic representation of the simulated elements for FP-PR, illustrated with the phantom's coronal plane: FP-PR field with beam direction (b1), range shifter (b2), phantom (b3), and FP detector (b4).

2.1 | Performance of the spot-wise energy selection algorithm

2.1.1 | FP-PR simulations

FP-PR simulations were performed for a HN phantom (Proton Therapy Dosimetry Head, model 731-HN by *Computerized Imaging Reference Systems, Inc.)*, using openREGGUI (openreggui.org),[28,29] with MCsquare as the Monte Carlo dose engine.[30] Nuclear interactions were turned on, and 10^8 primaries were used for each simulation.

Large FP-PR fields of 27 × 27 cm^2 for full phantom coverage (highlighted in orange in Figure 1), with a spot spacing of 5 mm, were simulated across the phantom in the x-y plane. The fields were directed toward the phantom from a gantry angle of 270 degrees (z axis). A water block of 40 mm acting as range shifter was simulated upstream of the phantom, and another water block of 8 mm of thickness at the exit of the phantom represented the FP detector (see Figure 1b). An isotropic dose grid of 1 mm was employed for dose calculations, and the two-dimensional FP signal (x-y plane) was extracted by integrating the dose volume in the water block representing the FP along the z axis.

The WEPL value corresponding to each pixel of the FP image was obtained based on a FP calibration dataset, which relates FP signal at different energies (the so-called ERDFs) to a set of known WETs. The calibration dataset, depicted in Figure S1, was simulated with a FP-PR imaging field with energy layers ranging from Emin = 70 MeV to Emax = 223 MeV, with energy steps of $\Delta E = 3$ MeV. Water-equivalent slabs of increasing thickness were simulated in steps of $\Delta X = 5$ mm, from 0 to 200 mm.

The assignment of each ERDF in a FP image to a WEPL value was performed by an optimization process that minimized the squared difference (L2 norm) between each ERDF in the FP image and the ERDFs in the FP calibration dataset.[26] More information on the calibration dataset and the optimization process can be found in the supplementary material.

Conventional FP-PRs, named "**reference FP-PR**," were simulated with a uniform FP-PR field with the same characteristics as the PR field used for calibration ($\Delta E = 3$ MeV, from Emin = 70 MeV to Emax = 223 MeV),

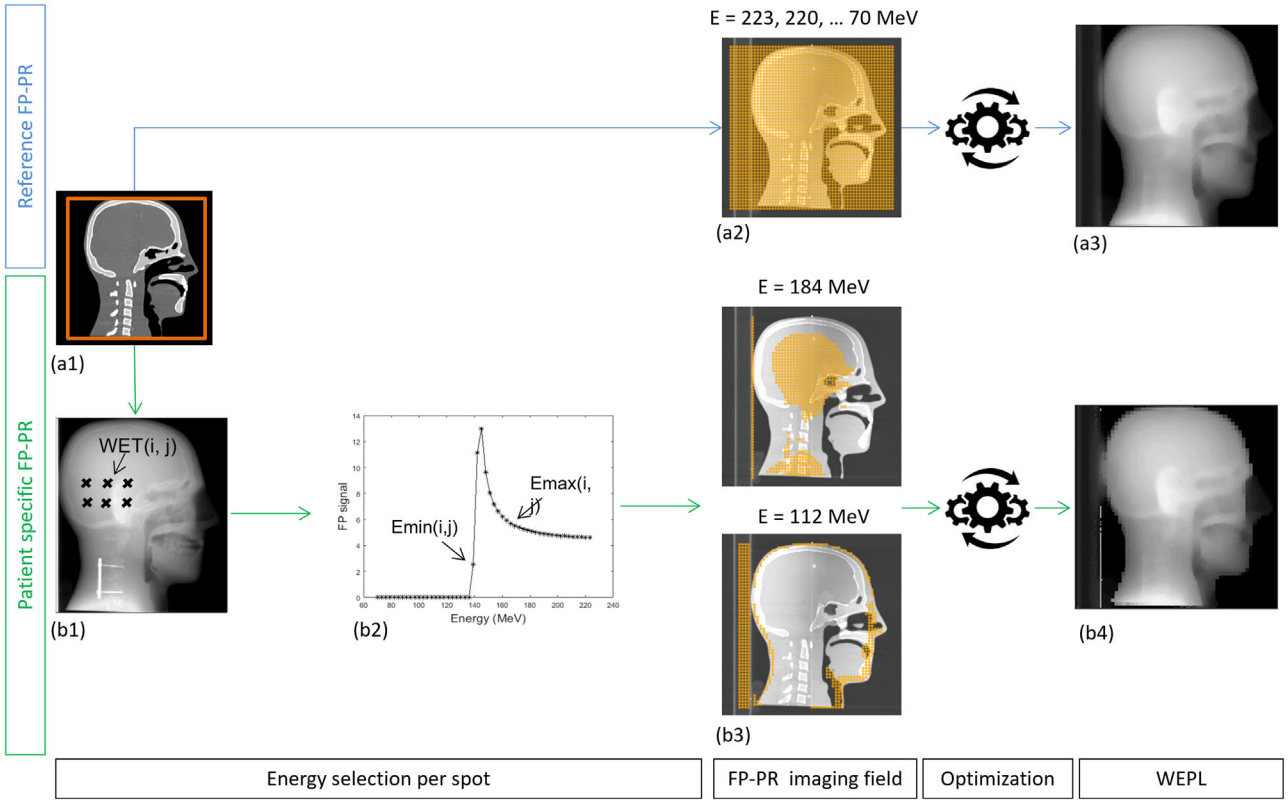

FIGURE 2 Simulation of reference and patient specific FP-PRs (blue and green branches, respectively). Both FP-PRs were simulated for the CT scan, where the edges of the FP-PR field are highlighted in orange (a1). For the reference FP-PR, all the energy layers of the imaging field were uniform (a2). The resulting FP signal was subject to an optimization process to obtain the corresponding WEPL map (a3). The determination of a patient specific FP-PR required the calculation of a WET map (b1), in which WET(i,j) values per spot coordinate (i,j) were extracted. Six illustrative spot coordinates are depicted by black crosses. The FP calibration dataset was used to find the ERDF(i,j) shown in b2, corresponding to WET(i,j). Emin(i,j) was identified in ERDF(i,j) as the first energy at which a non-zero FP signal was detected, and Emax(i,j) was calculated starting from Emin(i,j), according to $\Delta E = 3$ MeV and $n = 10$. The patient specific FP-PR imaging field consisted of non-uniform energy layers from 223 to 70 MeV. Spot patterns for two illustrative energy layers are shown in (b3). The resulting FP signal was introduced into the optimization process to obtain a patient specific WEPL map, exemplified for $n = 10$ (b4).

containing a total of 52 energy layers. The blue branch in Figure 2 represents the acquisition of a reference FP-PR imaging field (Figure 2a2) as well as the resulting WEPL map (Figure 2a3).

"Patient specific FP-PRs" were generated with an energy selection algorithm per spot coordinate, developed to create FP-PR imaging fields tailored to the phantom anatomy. An estimation of the lowest energy needed to pass through the phantom was performed for each spot coordinate (i,j), and the number of energies "n" used per spot coordinate was limited to certain values.

The tasks carried out to obtain patient specific FP-PRs are connected with green arrows in Figure 2, from (b1) to (b4). In the first step, a CT scan is used to calculate a WET map, from the same gantry angle in which the FP-PR field was directed (Figure 2b1). The WET value corresponding to each spot coordinate, referred in Figure 2b1 as WET(i,j), was extracted by averaging WET values over an area of 5×5 mm^2.

In the next stage, the FP calibration dataset is used to find the lowest energy, Emin(i,j), at which a non-zero FP signal would be obtained for a certain WET(i,j) (see Figure 2b2 and Figure S1). Given that the FP calibration contains ERDFs for a discrete number of WETs, a linear interpolation between ERDFs was performed for WET(i,j) values not present in the FP calibration dataset.

Figure 2b2 represents the assignment of a WET(i,j) to an ERDF, in which Emin(i,j) = 142 MeV. Starting from Emin(i,j), subsequent higher energies were determined in accordance with $\Delta E = 3$ MeV. The highest energy per spot coordinate, Emax(i,j), was obtained in accordance with a pre-selected number of energies (n) per spot coordinate in the imaging field.

The energy selection procedure per spot coordinate resulted in non-uniform energy layers (Figure 2b3) in the imaging field, where the presence of spot coordinates in each layer varied in accordance with the anatomy. High/low energies were assigned to regions of high/low WET (see Figure 2b3). The information about spot coordinates present in each energy layer was transferred to MCsquare and patient specific FP-PRs were obtained. Unlike with the reference FP-PR, where the

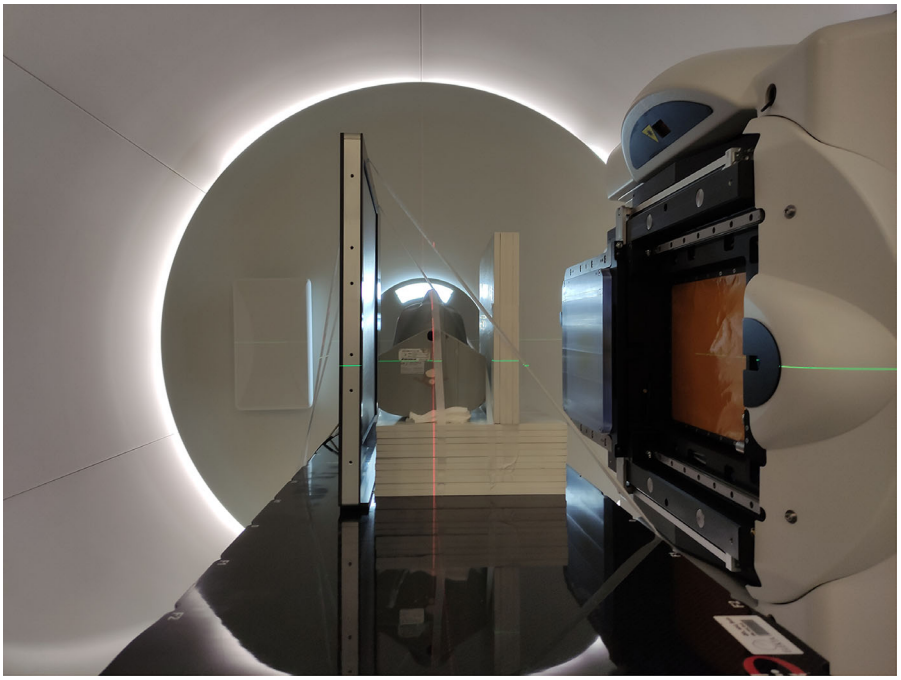

FIGURE 3 Experimental setup for FP-PR acquisition, from a gantry angle of 90°. PR fields were directed from right to left, encountering a stack of 4 cm of RW3 slabs (acting as range shifter), the HN phantom and the FP detector.

complete FP calibration dataset was employed in the optimization process to determine WEPL, the determination of WEPL values for patient specific FP-PRs was performed using only calibration ERDFs up to Emax(i,j).

Thirteen patient specific FP-PR simulations were performed, employing the energy selection algorithm for n = 26, 24, 22, 20, 18, 16, 14, 12, 10, 8, 6, 4, and 2.

2.1.2 | FP-PR measurements

In addition to the simulated data, a reference and a patient specific FP-PR (n = 10) were acquired experimentally using the same phantom and settings as described in Section 2.1.1., from a gantry angle of 90°. The experimental setup for the acquisitions is shown in Figure 3, which shows the FP detector used in the experiments (Phoenix, IBA Dosimetry, Schwarzenbruck, DE[31,32]). The phantom was aligned using in-room CBCT images, and FP images were acquired using a single shot mode (one energy layer per shot). The 2D signal provided by the FP contained pixels with a size of 0.2×0.2 mm^2. Each spot was set with 0.1 monitor units, carrying a dose between 200 and 300 cGy for the reference FP-PR and between 50 and 60 cGy for the patient specific FP-PR.

A calibration dataset with the same features as the simulated calibration was measured with the FP detector, using RW3 slabs of increasing thickness. This calibration was employed as input for the energy selection algorithm to generate the patient specific FP-PR field, as well as to reconstruct WEPL maps.

2.1.3 | Quantification

To quantify the impact of the energy selection algorithm on WEPL images, a comparison was performed between patient specific FP-PRs against the reference FP-PR. This comparison was performed for both simulated and measured FP-PRs. The absolute WEPL difference was calculated for each pixel of the WEPL maps, with respect to the WEPL values obtained from the reference FP-PR. Furthermore, mean absolute differences (MAD) were computed for each WEPL map.

2.2 | WEPL accuracy assessment of patient specific FP-PRs

FP-PRs were evaluated against MLIC-PRs to analyze the impact of the energy selection algorithm in terms of WEPL accuracy. MLIC-PRs are taken as ground truth in terms of WEPL accuracy.

2.2.1 | MLIC-PR and FP-PR simulations

MLIC-PRs were simulated across the base of skull, neck and brain regions of the phantom, covering areas of

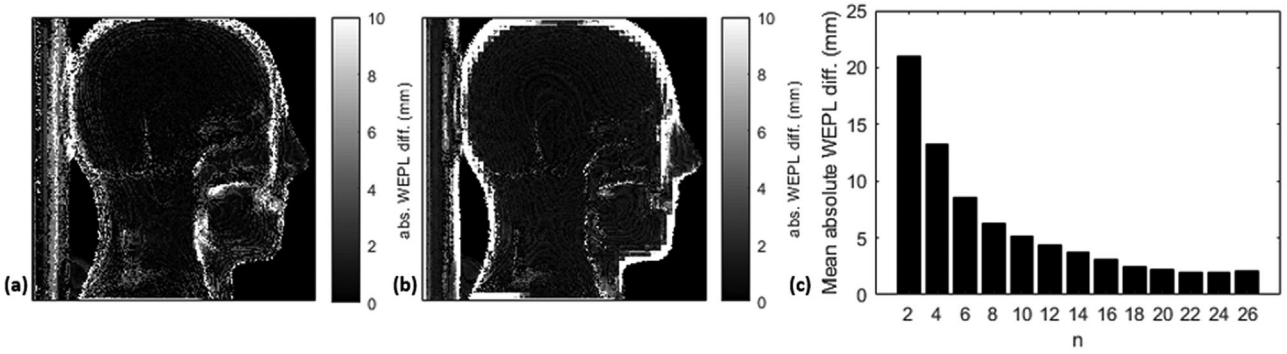

FIGURE 4 (a,b) Absolute WEPL difference maps obtained from a comparison between simulations of a reference FP and patient specific FP-PR with n = 20 (a) and n = 10 (b). (c) Mean absolute WEPL difference (mm) of patient specific FP-PRs simulated across the phantom with varying n with respect to the reference FP-PR.

4×4 cm^2 as shown in green in Figure 1a. The energy used for MLIC-PR simulations was 210 MeV and the gantry angle was 270°. The MLIC detector was represented at the beam exit of the phantom by a water block of 30 cm of thickness. Residual integral depth dose profiles were extracted by integrating the dose volume in the MLIC in x and y directions, obtaining a depth-dose MLIC signal along the beam direction (z axis).[13,21] An isotropic dose grid of 1 mm was employed, and MLIC-PR WEPL values were obtained using the pull-back method with respect to a simulated MLIC measurement in air.[22,24,26]

Total 13 patient specific FP-PRs, with n = 26, …, 2, were accordingly simulated in the same three regions where the MLIC-PRs were simulated, with a field size of 4×4 cm^2.

2.2.2 | MLIC-PR and FP-PR measurements

On a further step, MLIC-PRs were measured across the base of skull, neck, and brain of the phantom using the Giraffe MLIC (IBA Dosimetry, Schwarzenbruck, DE), with a gantry angle of 90°, a spot spacing of 5 mm and 0.012 monitor units per spot. The measured MLIC-PRs were compared against measured FP-PRs (reference and patient specific with n = 10).

The FP-PR measurements correspond to the data previously measured in Section 2.1.2. 4×4 cm^2 regions in the base of skull, neck, and brain were cropped out of the measured 27×27 cm^2 FP-PRs.

2.2.3 | Quantification

To quantify WEPL accuracy, mean relative WEPL errors (MRE) and standard deviations were computed between simulated MLIC-PR and FP-PRs, as well as for measured MLIC-PR and FP-PRs. FP-PR WEPL maps were down sampled via pixel averaging to match the resolution of MLIC-PR WEPL maps.

3 | RESULTS

3.1 | Performance of the spot-wise energy selection algorithm

Figure 4 shows two exemplary absolute WEPL difference maps between simulations of reference FP-PR and patient specific FP-PRs of the phantom, with n = 20 (Figure 4a) and n = 10 (Figure 4b). Generally, minimal WEPL absolute differences below 0.5 mm are found across the phantom anatomy. In regions in which lateral heterogeneities are present, such as the throat or the surface of the phantom, large WEPL absolute differences above 10 mm are observed.

A quantification of the MAD as a function of n is shown in Figure 4c. MADs increase as a function of decreasing n, from 2.1 mm (n = 26) to 21.0 mm (n = 2).

Figure 5a,b show phantom WEPL maps obtained experimentally, corresponding to a reference and a patient-specific FP-PR (n = 10), respectively. The absolute WEPL difference map obtained via measurements (Figure 5c) resulted in a MAD of 7.2 mm, 2 mm higher than the MAD (n = 10) obtained via simulations (5.2 mm).

3.2 | WEPL accuracy assessment of patient specific FP-PRs

Figure 6 shows the WEPL accuracy assessment carried out via FP-PR against MLIC-PR simulations in the base of skull, neck, and brain regions of the phantom. From n = 26 up to n = 10, MREs and standard deviations were mostly invariable and not affected by n, with values within $0.7 \pm 1.6\%$ in the base of skull, $0.2 \pm 1.0\%$ in the neck and $-0.4 \pm 0.6\%$ in the brain. Between n = 8 and n = 2, a steep increase in MRE was observed, with its highest values at $10.8 \pm 3.2\%$, $11.4 \pm 2.8\%$, and $7.9 \pm 1.4\%$ in the base of skull, neck and brain, respectively.

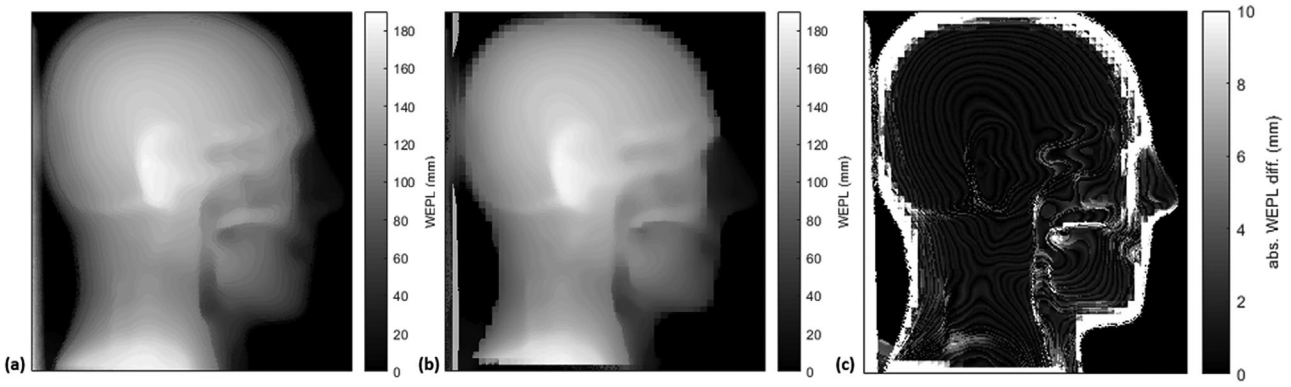

FIGURE 5 (a,b) WEPL maps acquired from reference and patient specific FP-PR measurements. (c): absolute WEPL difference map in mm, between (a) and (b).

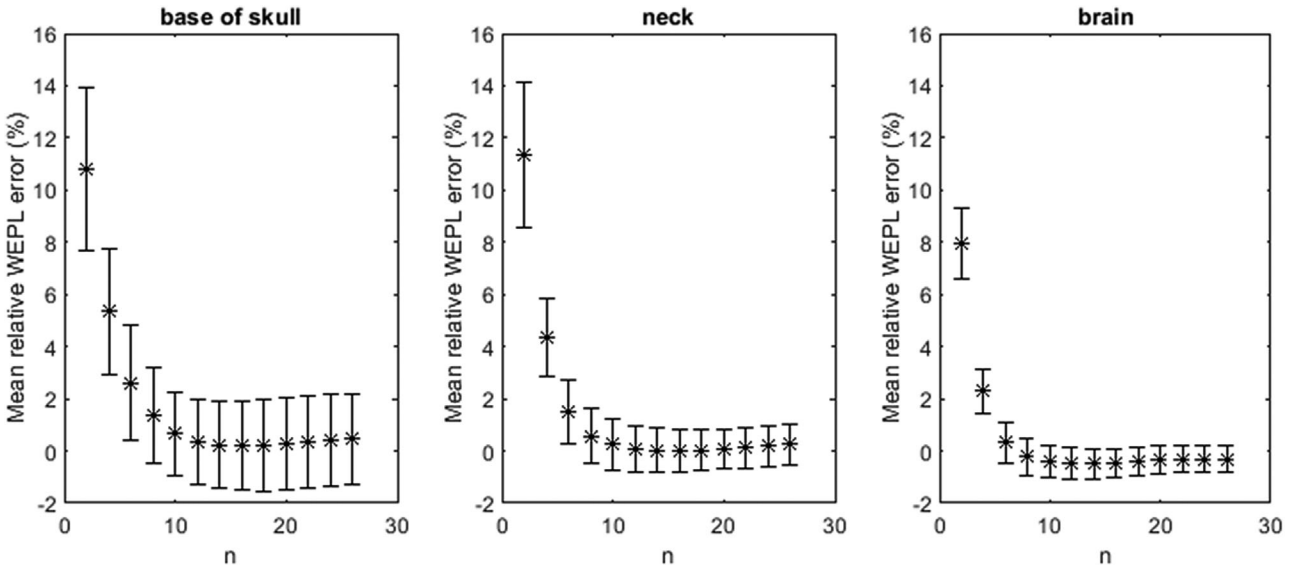

FIGURE 6 Mean relative WEPL error (%) and standard deviation (error bars) obtained from a comparison between patient specific FP-PR and MLIC-PR simulations in the base of the skull, brain and neck of the phantom, as a function of n.

The comparison of phantom FP-PRs against MLIC-PRs obtained experimentally resulted in MREs around $-1.3 \pm 2.0\%$, $-0.1 \pm 1.0\%$, $-0.1 \pm 0.4\%$ in the base of skull, neck, and brain, respectively (see Figure 7). Errors obtained from MLIC-PR against patient specific FP-PR were very similar to those obtained from a comparison against the reference FP-PR, with a difference below 0.3%.

4 | DISCUSSION

A method to perform FP-PRs using a patient specific imaging field with a reduced number of energies per spot coordinate selected in accordance with the anatomy has been established in silico and verified experimentally.

On a first step, the energy selection algorithm was presented and WEPL images resulting from patient specific FP-PRs were evaluated against reference FP-PRs. Absolute WEPL differences (Figures 4 and 5) between reference and patient specific FP-PRs were below 1 mm across the phantom anatomy, demonstrating the suitability of the energy selection procedure to provide WEPL images comparable to the reference FP-PR. This quantification highlighted potential limitations of the energy selection algorithm. For instance, large WEPL differences were observed in regions of sharp heterogeneities, especially in the surface of the phantom. The mismatch in WEPL values in the edges of the phantom is due to the WET averaging over areas of 5×5 mm^2 performed by the energy selection algorithm, which may result in a non-suitable energy selection if large heterogeneity gradients like air-bone are present.

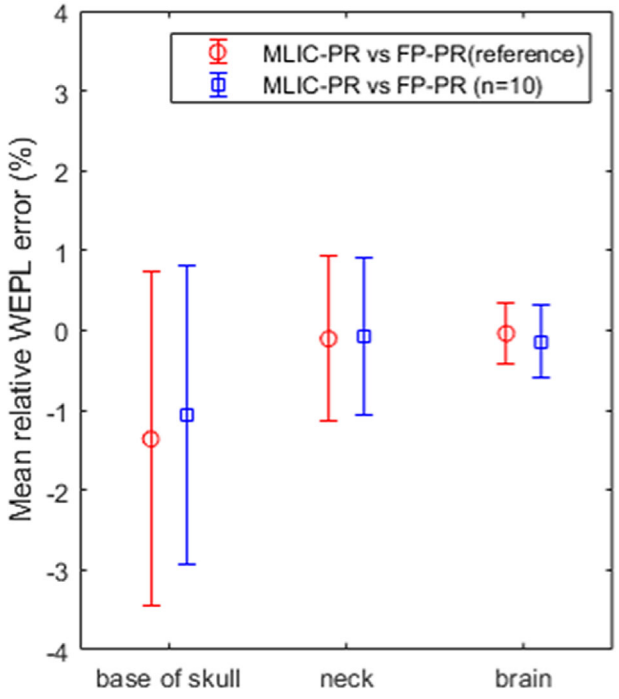

FIGURE 7 Mean relative WEPL error (%) and standard deviation (error bars) obtained experimentally between phantom MLIC-PR acquisitions and reference and patient specific FP-PR acquisitions, corresponding to red and blue data points, respectively.

This effect was also observed experimentally (Figure 5c) and gets magnified for lower values of n, as shown in Figure 4.

Secondly, WEPL accuracy of patient specific FP-PRs was evaluated by comparing such images against MLIC-PRs. Reduced and constant MREs below 1% were found between MLIC-PRs and patient specific FP-PR for $n \geq 10$, demonstrating that accurate FP-PRs can be performed in different anatomical regions with a low number of energies per spot (see Figure 6). Figure 7 shows experimental evidence that a similar WEPL accuracy can be obtained by delivering a reference or a patient specific FP-PR with $n = 10$. Furthermore, the MREs obtained via measurements were comparable to those simulated, with MRE differences below 0.5%. Several sources of uncertainty could have contributed to MREs obtained experimentally. MLIC-PRs and FP-PRs were acquired in different days, leading to phantom positioning discrepancies. Other uncertainties concern beam energy fluctuations, beam divergence, or FP positioning.[12,13]

In both phantom FP-PR simulations and measurements, MREs and standard deviations were slightly higher in the base of skull, followed by MREs in the neck and brain (see Figures 6 and 7). Such outcome can be explained by range mixing, given that the base of skull is the region with largest heterogeneities and thus sharpest WET gradients, while the brain is the most homogeneous region. An assessment of the impact of range mixing in WEPL accuracy could be a subject of future investigations. For the lowest n values, MREs tend toward high positive values (Figure 6), realizing a WEPL underestimation caused by an insufficient number of data points (energies) in the ERDFs.

In this study, experimental patient specific FP-PRs with $n = 10$ energy layers per spot showed an accuracy with MREs below 1%. The reduction of the number of energies was tackled in other studies by increasing ΔE, resulting in a loss of WEPL accuracy.[17,22,24,27] For instance, Alaka et al. reported systematic WEPL shifts when reducing the number of energy layers from 47 to 10, suggesting the need for an imaging field specific to the object to be imaged.[17] This work proposes an alternative method that does not increase the energy interval (3 MeV for both reference and patient specific FP-PRs). In this study ΔE remains unchanged, and for each spot coordinate, all the energies for which the beam is expected to stop inside the anatomy are excluded. Only the energies that are expected to contribute to the FP signal are delivered. Given that the most valuable information for the minimization process is the FP signal in the Bragg peak and its closest surroundings, data points in the plateau region of the Bragg peak (corresponding to the highest energies) were reduced by choosing a predefined n. As a result, similar WEPL accuracy was found in patient specific FP-PRs ($n = 10$) with respect to reference FP-PRs as well as MLIC-PRs.

Variations in the FP calibration settings affect WEPL accuracy. The calibration settings used in this work (ΔX and ΔE) were selected according to calibration setting optimality boundaries within which accurate WEPL measurements were feasible and practicable, as reported in a previous study.[26] Other settings such as spot spacing, the area over which WET(i,j) values are averaged, or the definition of Emin(i,j), could have an impact on WEPL accuracy. For instance, an increase on spot spacing might only be suitable for FP-PR images of homogeneous regions like the brain. If the region to be imaged is subject to substantial intra-fractional anatomical changes, a more conservative determination of Emin(i,j) with a margin toward lower energy values could be beneficial. To avoid WEPL inaccuracies due to inter-fractional changes, the energy selection algorithm could create a WET map from a weekly CT or even daily CBCT-based synthetic CT of the patient.[13]

The experimental acquisition of FP-PRs was time consuming (around 40 min per FP-PR) with respect to MLIC-PRs, given that the single shot FP acquisition mode required a delivery pause after each energy layer. In addition, the imaging fields covered the whole anatomy and thus contained 47 energy layers ($n = 10$), from 76 to 214 MeV, to achieve high WEPL accuracy for a wide range of WET values. To perform an in vivo PR acquisition in patients within the clinical workflow, the

acquisition time should be reduced to seconds, such that the whole PR procedure (including setup) does not take longer than 5 min.[12] Faster deliveries would be achieved if smaller regions are imaged (e.g., 10×10 cm^2 instead of 27×27 cm^2). The FP-PR acquisition procedure could be greatly reduced in time if future FP detector generations provide faster acquisition rates in movie mode, comparable to those available for MLIC acquisitions, thus avoiding interruptions after each energy layer.

MLIC-PRs, acquired with 0.012 monitor units per spot, carry a low imaging dose of 1 cGy, given that only one high energy is needed to obtain WEPL values.[12,13] In contrast, FP-PRs rely on multiple energies to measure accurate WEPL values. FP-PRs were measured with 0.1 monitor units due to familiarity with the detector response and acquisition settings at this dose level. Assuming that the FP detector could resolve images of PR fields with 0.012 monitor units per spot, a reference FP-PR would carry an imaging dose of around 35 cGy, while the dose of a patient specific FP-PR with n = 10 would be reduced below 7 cGy. An evaluation of the detector response and acquisition settings with low dose levels will be a subject of future investigations. The estimated FP-PR imaging dose is higher than the imaging dose of some list-mode PR detector configurations[33] and comparable to the dose given by some kV CBCT imaging systems.[34] Given that FP-PR is obtained with proton radiation, it could be accounted for in the proton therapy plan.

In contrast with MLIC-PR, FP-PR offers a more compact detector configuration. Challenges at different levels remain to be addressed to further investigate the suitability of FP-PR for in vivo range verification in adaptive proton therapy. Some of these challenges include delivery time reduction, possible limitations of the spatial resolution to detect different sources of range error, and integration in the treatment room to enable rotations. A FP detector suitable for proton and photon radiation could be mounted on the gantry system and integrated into the clinical workflow for x-ray alignment purposes as well as for in vivo range assessment by means of FP-PR.

Patient specific FP-PR acquisitions with the proposed spot-wise energy selection method provide a WEPL accuracy below 1% in the base of skull, neck, and brain regions, and hold the potential to serve as a quality control tool in online adaptive proton therapy workflows, detecting sources of range error such as patient misalignments, calibration curve errors, or anatomical changes.[10] Future investigations could evaluate the performance of the patient specific FP-PRs when a source of range error is introduced. Furthermore, the simultaneous detection of various sources of range error could be automated by means of artificial intelligence,[10] providing information to assist decisions about plan adaptation.

5 | CONCLUSION

A method to accurately measure WEPL by means of FP-PR with a reduced number of energies tailored to the patient anatomy has been established in silico and validated experimentally. Patient specific FP-PR holds the potential to assist online range verification quality control processes within adaptive proton therapy workflows.

ACKNOWLEDGEMENTS

This study was financially supported by a grant from the Dutch Cancer Society (KWF research project 11518), called “INCONTROL- Clinical Control Infrastructure for Proton Therapy Treatments.” The authors acknowledge openREGGUI for providing the tools used in this study.

CONFLICT OF INTEREST

Johannes A. Langendijk is a consultant for proton therapy equipment provider IBA. University of Groningen, University Medical Centre Groningen, Department of Radiation Oncology has active research agreements with RaySearch, Philips, IBA, Mirada, Orfit.

REFERENCES

1. Poludniowski G, Allinson NM, Evans PM. Proton radiography and tomography with application to proton therapy. *Brit J Radiol*. 2015;88:1-14. doi:10.1259/bjr.20150134
2. Schneider U, Pedroni E. Proton radiography as a tool for quality control in proton therapy. *Med Phys*. 1994;22(4):353-363. doi:10.1118/1.597470
3. Schneider U, Pemler P, Besserer J, Pedroni E, Lomax A, Kaser-Hotz B. Patient specific optimization of the relation between CT-Hounsfield units and proton stopping power with proton radiography. *Med Phys*. 2005;32(1):195-199. doi:10.1118/1.1833041
4. Knopf AC, Lomax A. In vivo proton range verification: a review. *Phys Med Biol*. 2013;58(15):131-160. doi:10.1088/0031-9155/58/15/R131
5. Doolan PJ, Testa M, Sharp G, Bentefour EH, Royle G, Lu HM. Patient-specific stopping power calibration for proton therapy planning based on single-detector proton radiography. *Phys Med Biol*. 2015;60(5):1901-1917. doi:10.1088/0031-9155/60/5/1901
6. Mumot M, Algranati C, Hartmann M, Schippers JM, Hug E, Lomax AJ. Proton range verification using a range probe: definition of concept and initial analysis. *Phys Med Biol*. 2010;55(16):4771-4782. doi:10.1088/0031-9155/55/16/010
7. Farace P, Righetto R, Meijers A. Pencil beam proton radiography using a multilayer ionization chamber. *Phys Med Biol*. 2016;61(11):4078-4087. doi:10.1088/0031-9155/61/11/4078
8. Meijers A, Free J, Wagenaar D, et al. Validation of the proton range accuracy and optimization of CT calibration curves utilizing range probing. *Phys Med Biol*. 2020;65(3), 03NT02. doi:10.1088/1361-6560/ab66e1
9. Sarosiek C, DeJongh EA, Coutrakon G, et al. Analysis of characteristics of images acquired with a prototype clinical proton radiography system. *Med Phys*. 2021;48(5):2271-2278. doi:10.1002/mp.14801
10. Seller Oria C, Guterres Marmitt G, Both S, Langendijk JA, Knopf AC, Meijers A. Classification of various sources of error in range assessment using proton radiography and neural networks in head and neck cancer patients. *Phys Med Biol*. 2020;65(23) 235009. doi:10.1088/1361-6560/abc09c
11. Parodi K, Polf JC. In vivo range verification in particle therapy. *Med Phys*. 2018;45(11):e1036-e1050. doi:10.1002/mp.12960

12. Meijers A, Seller Oria C, Free J, Langendijk JA, Knopf AC, Both S. Technical note: First report on an in vivo range probing quality control procedure for scanned proton beam therapy in head and neck cancer patients. *Med Phys*. 2021;48(3):1372-1380. doi:10.1002/mp.14713
13. Seller Oria C, Thummerer A, Free J, et al. Range probing as a quality control tool for CBCT based synthetic CTs: in vivo application for head and neck cancer patients. *Med Phys*. 2021;48:4498-4505. doi:10.1002/mp.15020
14. Talamonti C, Reggioli V, Bruzzi M, et al. Proton radiography for clinical applications. *Nucl Instrum Methods Phys Res A*. 2010;612(3):571-575. doi:10.1016/j.nima.2009.08.040
15. Johnson RP. Review of medical radiography and tomography with proton beams. *Rep Prog Phys*. 2018;81(1) 016701. doi:10.1088/1361-6633/aa8b1d
16. Zhang R, Jee KW, Cascio E, Sharp GC, Flanz JB, Lu HM. Improvement of single detector proton radiography by incorporating intensity of time-resolved dose rate functions. *Phys Med Biol*. 2017;63(1):015030. doi:10.1088/1361-6560/aa9913
17. Alaka BG, Bentefour EH, Chirvase C, Samuel D, Teo BKK. Feasibility of energy-resolved dose imaging technique in pencil beam scanning mode. *Biomed Phys Eng Express*. 2020;6(6):65009. doi:10.1088/2057-1976/abb4ed
18. Tendler I, Robertson D, Chinmay D, Rajesh P, Alsanea F. Image quality evaluation of projection- and depth dose-based approaches to integrating proton radiography using a monolithic scintillator detector. *Phys Med Biol*. 2021;66(14). doi:10.1088/1361-6560/ac0cc3
19. Jee KW, Zhang R, Bentefour EH, et al. Investigation of time-resolved proton radiography using x-ray flat-panel imaging system. *Phys Med Biol*. 2017;62(5):1905-1919. doi:10.1088/1361-6560/aa5a43
20. Hammi A, Placidi L, Weber DC, Lomax AJ. Positioning of head and neck patients for proton therapy using proton range probes: a proof of concept study. *Phys Med Biol*. 2018;63(1); 105025. doi:10.1088/1361-6560/aa9cff
21. Meijers A, Seller Oria C, Free J, et al. Assessment of range uncertainty in lung-like tissue using a porcine lung phantom and proton radiography. *Phys Med Biol*. 2020;65(15): 155014. doi:10.1088/1361-6560/ab91db
22. Harms J, Maloney L, Sohn JJ, Erickson A, Lin Y, Zhang R. Flat-panel imager energy-dependent proton radiography for a proton pencil-beam scanning system. *Phys Med Biol*. 2020;65(14):0-10. doi:10.1088/1361-6560/ab9981
23. Bentefour EH, Schnuerer R, Lu HM. Concept of proton radiography using energy resolved dose measurement. *Phys Med Biol*. 2016;61(16):N386-N393. doi:10.1088/0031-9155/61/16/N386
24. Huo W, Zwart T, Cooley J, et al. A single detector energy-resolved proton radiography system: a proof of principle study by Monte Carlo simulations. *Phys Med Biol*. 2019;64(2): 025016. doi:10.1088/1361-6560/aaf96f
25. Petterson M, Penfold S, Lee W. Relative Stopping Power (RSP) and Water Equivalent Thickness (WET) measurements of phantoms using x-ray flat panel detector and scanned proton beam. Poster, PTCOG58. Published 2019. Accessed August 30, 2022. https://www.protominternational.com/wp-content/uploads/2019/06/ptcog2019_v2_sm_at_sp.pdf
26. Seller Oria C, Guterres Marmitt G, Free J, et al. Optimizing calibration settings for accurate water equivalent path length assessment using flat panel proton radiography. *Phys Med Biol*. 2021;66: 21NT02.
27. van der Heyden B, Cohilis M, Souris K, de Freitas Nascimento L, Sterpin E. Artificial intelligence supported single detector multi-energy proton radiography system. *Phys Med Biol*. 2021;66(10): 105001. doi:10.1088/1361-6560/abe918
28. Deffet S, Macq B, Righetto R, vander Stappen F, Farace P. Registration of pencil beam proton radiography data with x-ray CT. *Med Phys*. 2017;44(10):5393-5401. doi:10.1002/mp.12497
29. Deffet S, Cohilis M, Souris K, et al. openPR—a computational tool for CT conversion assessment with proton radiography. *Med Phys*. 2021;48(1):387-396. doi:10.1002/mp.14571
30. Souris K, Lee JA, Sterpin E. Fast multipurpose Monte Carlo simulation for proton therapy using multi- and many-core CPU architectures. *Med Phys*. 2016;43(4):1700-1712. doi:10.1118/1.4943377
31. Su Z, Hsi W, Forthomme J, Rossomme S. Evaluations of a flat-panel based compact daily quality assurance device for proton pencil beam scanning (PBS) system. *Phys Med*. 2020;80:243-250. doi:10.1016/J.EJMP.2020.10.026
32. IBA Dosimetry: myQA® Phoenix - Digital detector array. Accessed March 23, 2022. https://www.iba-dosimetry.com/product/myqa-phoenix
33. DeJongh EA, DeJongh DF, Polnyi I, et al. Technical note: a fast and monolithic prototype clinical proton radiography system optimized for pencil beam scanning. *Med Phys*. 2021;48(3):1356-1364. doi:10.1002/mp.14700
34. Alaei P, Spezi E. Imaging dose from cone beam computed tomography in radiation therapy. *Phys Med*. 2015;31(7):647-658. doi:10.1016/j.ejmp.2015.06.003

SUPPORTING INFORMATION

Additional supporting information can be found online in the Supporting Information section at the end of this article.

How to cite this article: Seller Oria C, Free J, Marmitt GG, et al. Technical note: Flat panel proton radiography with a patient specific imaging field for accurate WEPL assessment. *Med Phys*. 2023;50:1756–1765. https://doi.org/10.1002/mp.16208